

Multiple Wavepacket Decomposition of F404 Engine

Military Jet Noise

Tyce W. Olaveson¹ and Kent L. Gee²

Brigham Young University, Provo, Utah, 84602, USA

Noise sources in heated, supersonic jets are challenging to measure directly due to the extreme environment. Inverse methods, such as acoustic beamforming, using data collected near these sources can be used to construct equivalent source models that accurately describe the acoustic radiation. However, generating these models for a complex source can require thousands of parameters for a complete description. To address this challenge, a multiple wavepacket decomposition is introduced, reducing the source into a set of analytic wavepackets that recreate the full-rank model. This paper provides an overview of the decomposition procedure and applies it to acoustic data collected near a T-7A-installed GE F404 engine. The decomposition is validated for a peak frequency at military power and physical implications are discussed. It is shown that the downstream radiation at MIL can be accurately reconstructed with as few as five wavepackets with minimal error. The number of wavepackets required to capture the primary radiation region tends to increase with frequency and engine power. Beyond the dominant frequencies, the number of wavepackets per wavelength increases drastically, indicating a rapid decrease in source coherence. Finally, a single wavepacket model is fit to the data at MIL, which captures primary radiation features.

I. Nomenclature

а	= Wavepacket amplitude	$q_{wpkt}(x)$	= Analytic wavepacket
c_{1}, c_{2}	= Wavepacket growth and decay rates	Q_{HM}	= Equivalent source model from HM
C	= Cross spectral matrix	Q_{MWP}^n	= MWP model with n wavepackets.
D	= Jet exit diameter	Q_z	= Residual matrix
f	= frequency	r	= Position vector
G	= Green's function matrix	R	= Residual subspace matrix
<u>G</u>	= Regularized Green's function matrix	S	= Number of presumed sources in HM
k_{peak}	= Wavepacket wavenumber	Sr	= Strouhal number, $Sr = fD/u_j$
\boldsymbol{L}	= Regularization matrix	u	= Source trial vector
M	= Number of measurement locations	u_i	= jet exit velocity
n	= Number of wavepackets	w	= singular vector
p	= Pressure vector	w	= Scaled singular vector
\boldsymbol{P}_{MUSIC}	= Music power vector	W	= Singular vector matrix of \mathbf{Q}_z
q	= Source strength vector	x_{ref}	= Wavepacket center point
$oldsymbol{q}_{part}$	= Partial source vector	δ	= Penalization parameter

¹ Doctoral Candidate, Department of Physics and Astronomy. Student Member AIAA

² Professor, Department of Physics and Astronomy. Associate Fellow AIAA.

 Λ = Singular value matrix

II. Introduction

Sound levels produced by high-performance military aircraft pose a risk of hearing loss to nearby launch personnel [1]. For this purpose, significant work has been done to characterize the radiation properties of jets, as well as investigate potential noise reduction technology [2]. One method of source characterization comes in the form of acoustic beamforming. The goal of classical beamforming algorithms is to determine the spatial location and strength of an acoustic source. Merino et al. [3] provide a comprehensive review of some common algorithms including their applications and limitations. Beyond this set, other advanced methods have been developed. Of note is the hybrid beamforming method presented by Padois et al. [4], which is reviewed more completely in Section IV.A. This method was used by Harker et al. [5] to characterize noise radiation from an F-22 and by Olaveson et al. [6] on the T-7A to investigate the behavior of dual-lobe radiation phenomena.

One challenge with these beamforming approaches is the resultant equivalent source models (ESMs) tend to be large and require special processing at individual frequencies. While the frequency issue is not easily avoided, many methods have appeared to reduce the complexity of these models. One of these is the proper orthogonal decomposition (POD) [7] which approaches the equivalent source description by decomposing the flow into a set of orthogonal spatial modes with time dependent coefficients. This method's objective is to represent the most energy in the flow with the fewest number of basis functions. An expansion of this method is spectral POD (SPOD) [8], which generalizes the basis functions to include a frequency dependence. This method has seen extensive use in many fluid-based analyses [9] and has been used to connect energy modes to self-coherent wavepacket-like structures [10].

The presence of coherent structures in jet turbulence has been known since 1971 [11]. These structures are important contributors to acoustic radiation and provide a strong starting point for modeling physical flow. Jordan et al. [12] provide an overview of turbulent wavepackets and show that they accurately describe low-angle radiation from high-subsonic and low supersonic jets. Cavalieri et al. [13] introduce a time-dependent 'jitter' that accounts for the temporal intermittency or 'puffs' of energy described by Crow and Champagne [11] and seen in experiment [14]. While these wavepackets have been used primarily to describe turbulent structures, an alternate approach uses a wavepacket-like distribution of sources to model the acoustic radiation directly. This type of method was applied by Papamoschou [15] who used a set of six azimuthal wavepackets to describe the far-field radiation of high subsonic jets. In terms of supersonic, heated jets, a single wavepacket model has been applied to full-scale aircraft to match near-field intensities [16].

This work combines the equivalent source models of beamforming with the physically relevant wavepacket models to produce a reduced order model of an acoustically equivalent source. This method was developed by Harker [17] and validated against noise from a high-performance jet aircraft, the results of which were documented in a single conference proceedings [18]. This paper applies the multiple wavepacket decomposition to near-field data collected near an F404 engine installed on a T-7A aircraft. Section III describes the relevant parts of that experiment, Section IV reviews the hybrid beamforming method and provides a detailed explanation of the multiple wavepacket decomposition procedure. Finally, a discussion on the implications of this decomposition is included in Section V.

III. Experiment

The analysis in this paper uses a portion of the T-7A dataset. This experiment was conducted in the early hours of August 18th, 2019, at Holloman Air Force Base in New Mexico. The aircraft was installed with an F404 engine and tethered to the runway. The measurement featured over 200 microphones arranged in near and far-field arrays. This paper uses the data collected at the near-field imaging array, which was made of 120 GRAS 46BD and 46BG ¼" pressure microphones. The array, shown in Fig. 1, ran parallel to the jet centerline in the forward direction and then parallel to the expected shear layer downstream of the nozzle. Each microphone was taped to the ground to facilitate the removal of ground reflections (assumed to be a pressure doubling at the ground interface). The inter-element spacing was varied across the array with smaller intervals near the sideline and longer ones at the ends of the array. This was done in anticipation of the expected spectral behavior of the jet noise in each direction, low frequencies at shallow angles, and high frequencies to the sideline. This same array has been used in several other studies on jet noise source characterization of military aircraft [19, 20, 21].

The aircraft was cycled through six engine conditions, but only the four highest engine conditions are analyzed in this paper: 38% thrust, 55% thrust, military power (MIL, 100% thrust) and full afterburner (AB). Each condition was

held long enough to allow for at least 30 seconds of steady-state data to be recorded. This cycle was then repeated six times and spectral data averaged across runs. Further details on this measurement are included in Ref [22].

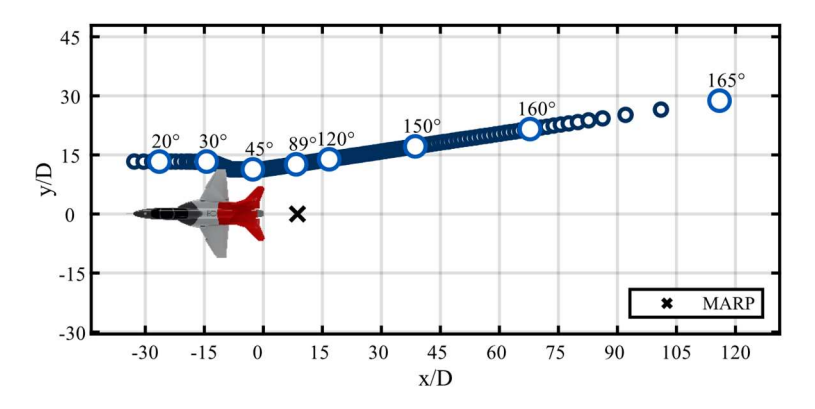


Figure 1. Schematic of the T-7A near-field imaging array.

IV. Methods

A. Hybrid Beamforming

The first step in the decomposition requires a mathematical representation of the sound source. Such an equivalent source model (ESM) is generally obtained through holography or beamforming methods. This paper uses the Hybrid Beamforming method (HM) as presented by Padois et al. [4], which assigns cross-spectral amplitudes to a collection of monopoles. This advantage to the cross-spectral approach is that all the inter-source information, such as coherence, is baked into the ESM. While a complete description of the method is not provided here, an overview is included for completion.

The Hybrid Method aims to reduce measured spectral information to a collection of monopoles that recreate the data as closely as possible. In essence, it solves the inverse problem given by

$$p(\omega) = G(\mathbf{r}_m, \mathbf{r}_s | \omega) q(\omega) \tag{1}$$

where p and q are the (frequency-dependent) pressures and source amplitudes respectively, and G is the Green's function that connects the sources at r_s to the field locations at r_m with the frequency ω . In practice, each term is a matrix or vector: $\mathbf{p} \in \mathbb{C}^{M \times 1}$, $\mathbf{G} \in \mathbb{C}^{M \times S}$, and $\mathbf{q} \in \mathbb{C}^{S \times 1}$ where M is the number of measurement locations and S is the number of presumed sources. Given the source distribution q, the pressure p at a new set of field locations, r_f , can be calculated using a new Green's function $G(r_f, r_s | \omega)$. This work assumes a free-field Green's matrix with elements $G_{ij} = \frac{j\rho ck}{4\pi\Delta r_{ij}} e^{-jk\Delta r_{ij}}$ where $\Delta r_{ij} = ||r_i - r_j||_2$ is the Euclidean distance between the i^{th} source and the j^{th} measurement (or field) location.

By requiring that the number of sources be larger than the number of measurement locations, Eq. (1) is overdetermined and can be solved using a least-squares approach. The (modified) solution to the least-squares problem can be cast as

$$\mathbf{q}_{\lambda\beta} = \operatorname{argmin}\{||\beta \mathbf{p} - \mathbf{G}\mathbf{q}||_{2}^{2} + \lambda^{2} \Omega(\mathbf{p})^{2}\}$$
 (2)

where λ is a regularization parameter and $\Omega(\cdot)$ is a smoothing norm designed to prevent the system from becoming numerically unstable [4]. The scalar β is included to account for potential over-regularization. In HM, the smoothing norm is taken as $\Omega(q) = ||Lq||_2$, where L is a regularization matrix that will be discussed later. The solution to Eq. (2) is found by taking a derivative with respect to q and setting the cost to zero:

$$\mathbf{q}_{\lambda\beta} = \mathbf{L}^{-1} \left(\mathbf{\underline{G}}^{\mathcal{H}} \mathbf{\underline{G}} + \lambda^2 \mathbf{I} \right)^{-1} \mathbf{\underline{G}}^{\mathcal{H}} \beta \mathbf{p}$$
 (3)

where $(\cdot)^{\mathcal{H}}$ is the Hermitian transpose and $\mathbf{G} = \mathbf{G}\mathbf{L}^{-1}$ is the regularized Green's function.

In classic delay-and-sum beamforming, the measurement array is assumed to be linear, however, other array geometries are valid and, in many cases, address specific aspects of the noise source. To allow for a generic array geometry, Padois et al. [4] introduce the weight matrix $W_{ij} = G_{ij}/g_j^{\mathcal{H}}g_j$ where g_j is the j^{th} column of the Green's matrix, which describes how the measurement array responds to the j^{th} monopole. Collectively, these functions are used to describe the beamforming response $q_{BF} = W^{\mathcal{H}}p$. The regularization matrix is now expressed as:

$$L^{-1} = diag\left(\frac{|\boldsymbol{q}_{BF}|}{||\boldsymbol{q}_{RF}||_{\infty}}\right) \tag{4}$$

where $|\cdot|$ is elementwise absolute value and $||\cdot||_{\infty}$ is the infinity norm. The expression $diag(\cdot)$ generates a square matrix by casting the vector argument along the main diagonal.

The next step is to reformulate the problem in terms of the cross spectral matrix, which is defined as $C = pp^{\mathcal{H}}$. The beamforming response is then $Q_{BF} = q_{BF}q_{BF}^{\mathcal{H}} = W^{\mathcal{H}}CW$, and finally the regularization matrix is $L^{-1} = diag\left(\sqrt{\frac{Diag(Q_{BF})}{||Diag(Q_{BF})||_{\infty}}}\right)$ where $Diag(\cdot)$ creates a vector out of the main diagonal of the matrix argument. Additionally, since L is defined in terms of W, the regularized Green's matrix is also redefined as $G = WL^{-1}$.

The cross-spectral solution is then derived as

$$\mathbf{Q}_{\lambda\beta} = \mathbf{q}_{\lambda\beta} \mathbf{q}_{\lambda\beta}^{\mathcal{H}} \tag{5}$$

$$= L^{-1} (\underline{\boldsymbol{G}}^{\mathcal{H}} \underline{\boldsymbol{G}} + \lambda^{2} \boldsymbol{I})^{-1} \underline{\boldsymbol{G}}^{\mathcal{H}} \beta \boldsymbol{p} \left(L^{-1} (\underline{\boldsymbol{G}}^{\mathcal{H}} \underline{\boldsymbol{G}} + \lambda^{2} \boldsymbol{I})^{-1} \underline{\boldsymbol{G}}^{\mathcal{H}} \beta \boldsymbol{p} \right)^{\mathcal{H}}$$
(6)

$$= \mathbf{L}^{-1} \mathbf{J}_{\lambda} \mathbf{G}^{\mathcal{H}} \beta \mathbf{p} (L^{-1} \mathbf{J}_{\lambda} \mathbf{G}^{\mathcal{H}} \beta \mathbf{p})^{\mathcal{H}}, \text{ for } \mathbf{J}_{\lambda} = (\mathbf{G}^{\mathcal{H}} \mathbf{G} + \lambda^{2} \mathbf{I})^{-1}$$
(7)

$$= L^{-1} J_{\lambda} \underline{\mathbf{G}}^{\mathcal{H}} \beta \mathbf{p} \mathbf{p}^{\mathcal{H}} \beta^{\mathcal{H}} \underline{\mathbf{G}} J_{\lambda}^{\mathcal{H}} (L^{-1})^{\mathcal{H}}$$
(8)

$$\mathbf{Q}_{\lambda\beta} = \mathbf{L}^{-1}\beta \mathbf{J}_{\lambda}\mathbf{G}^{\mathcal{H}}\mathbf{C}\mathbf{G}\mathbf{J}_{\lambda}^{\mathcal{H}}\beta^{\mathcal{H}}(\mathbf{L}^{-1})^{\mathcal{H}}$$
(9)

Equation (9) is the Hybrid Method (HM), which can be thought of as a 'backpropagation' from the measurement array to the proposed set of monopoles. The parameters λ and β are explored more fully in Padois et al. [4] This work uses $\lambda = 0.05 \max\{eig(\underline{G}^{\mathcal{H}}\underline{G})\}\$ as in Ref. [5] and $\beta = ||\underline{G}^{\mathcal{H}}\underline{G} + \lambda^2 I||_2$, which helps regularize the computation of J_{λ} , which requires a matrix inverse.

The HM output is the complex matrix Q_{HM} (the subscript $\lambda\beta$ has been replaced with HM) that gives the amplitudes of the sources as well as cross spectral properties including the coherence. This constitutes an equivalent source model for the measured data. From here, the cross-spectral matrix can be calculated at any new set of field locations using:

$$\mathbf{C} = \mathbf{p}\mathbf{p}^{\mathcal{H}} \tag{10}$$

$$= Gqq^{\mathcal{H}}G^{\mathcal{H}} \tag{11}$$

$$\mathbf{C} = \mathbf{G}\mathbf{Q}_{HM}\mathbf{G}^{\mathcal{H}},\tag{12}$$

where G is now the Green's matrix connecting the locations of the equivalent sources to the desired field locations.

B. Multiple Wavepacket Decomposition

The ESM derived from HM is an adequately sufficient model of the acoustic source. However, the matrix description contains S^2 complex values for each frequency of interest. A reduced order model could be effectuated using a singular value decomposition (SVD) and only keeping the top l components, resulting in a model with lS parameters for each frequency. One challenge with this approach is that the singular vectors are not necessarily physically significant. The multiple wavepacket (MWP) decomposition combines the SVD approach with a set of

basis functions created from an asymmetric-Gaussian shaped wavepacket ansatz with 5 parameters. This type of decomposition not only has a stronger physical meaning, but it further reduces the number of parameters to 5n for n wavepackets. The resultant MWP decomposition describes the source in terms of a set of continuous functions, which can be used to increase the spatial resolution of the ESM. This decomposition follows an iterative approach, where each wavepacket is extracted from the beamformed ESM, Q_{HM} . The following subsections explain each of the steps in the process. A more complete description is given by Harker [17].

1. Initialization

The first step is to initialize the full rank matrix, Q_{HM} , as Q_z where Q_z represents the running residual of the decomposition and will be repeatedly updated as each wavepacket is generated.

2. Calculate the MUSIC power

The process of decomposing Q_z into a collection of analytic wavepackets is done iteratively by extracting one wavepacket at a time. The first step is to calculate the Multiple Signal Classification (MUSIC) power [23] which identifies the optimal source location. This is done by computing the singular value decomposition of the running residual:

$$\mathbf{Q}_{z} = \mathbf{W} \, \mathbf{\Lambda} \, \mathbf{W}^{\mathcal{H}}, \tag{13}$$

where the unitary matrix W is composed of the singular vectors, w_i , and Λ is the diagonal matrix of singular values. The matrix Q_z can be decomposed into a signal subspace and a residual subspace. The signal subspace represents the most prominent contributions to the full matrix and is spanned by the largest singular vectors. The residual subspace is formed the rest of the singular vectors as

$$\mathbf{R} = \sum_{p=l+1}^{S} \mathbf{w}_p \mathbf{w}_p^{\mathcal{H}}.$$
 (14)

Since the MWP decomposition extracts a single wavepacket at a time, l is set to 1 so that the signal space is spanned by the largest singular vector.

The MUSIC power seeks to define a partial source that best describes the coherent energy in the full sources. This is done indirectly using the residual subspace. First, a trial vector \mathbf{u}_i is constructed which represents a possible distribution of sources at the known locations given by $\mathbf{r}_{i,\text{ref}}$. The MUSIC power for this source distribution then calculated by

$$P_{\text{MUSIC},i} = \frac{1}{\boldsymbol{u}_{i}^{\mathcal{H}} \boldsymbol{R} \boldsymbol{u}_{i}}.$$
 (15)

It should be noted that if the trial vector is a singular vector describing the signal subspace then $P_{\text{MUSIC}} = \infty$ since each singular vector is perfectly coherent with itself. For the purposes of this paper, the MUSIC power is used to identify the best location for the peak of an analytic wavepacket, thus the trial source distribution corresponds to one of the monopoles used in the HM source description, i.e. $u_i = [0, ..., 1, ..., 0]^T$. In this formulation, the denominator of (15) reduces to simply pulling out the main diagonal of \mathbf{R} and $\mathbf{P}_{\text{MUSIC}} = 1/\text{diag}(\mathbf{R})$, where division is done element wise. Thus, the optimal location for a monopole, $\mathbf{r}_{i,\text{ref}}$, corresponds to where the residual subspace has a minimum.

The final step is to calculate a partial source that describes the coherent energy in Q_z . This is done by taking the i_{ref} th row of W, which corresponds to the i_{ref} th element of each singular vector and call this $v = [w_{1,i,ref}, ..., w_{S,i,ref}]$. This vector is then multiplied by W and scaled by the corresponding element in Q_z . This partial source is calculated as:

$$q_{part} = \frac{Wv^{\mathcal{H}}}{\sqrt{Q_{zi_{ref},i_{ref}}}}.$$
(16)

This partial source describes the portion of \boldsymbol{Q}_z that is coherent with the source at $\boldsymbol{r}_{l,\mathrm{ref}}$.

3. Fit the partial source to an analytic wavepacket

Once the partial source has been extracted, it is then ready to be fit to a wavepacket. In many cases, the distribution of source amplitudes is similar to the asymmetric Gaussian function in Eq. (17).

$$q_{wpkt}(x) = a \exp\left(-4 \ln 2 \frac{\left(x - x_{ref}\right)^2}{c_i^2} + j\left(k_{peak}x\right)\right), c_i = \begin{cases} c_1, x < x_{ref} \\ c_2, x \ge x_{ref} \end{cases}$$
(17)

This wavepacket is defined by five parameters: a, c_1, c_2, x_{ref} , and k_{peak} which describe the amplitude, growth rate, decay rate, center location, and wavenumber, respectively. Example wavepackets are plotted in Fig. 2 for two different sets of parameters. The amplitude is set to unity (a = 1) in anticipation of the later optimization that will be used to match the true source levels. The growth and decay rates $(c_1 \text{ and } c_2)$ are equivalent measures of the full-width half maximum value for the upstream and downstream components of q_{part} . These are obtained by doubling the spatial distance between x_{ref} and the nearest half-maximum point. The center of the wavepacket is given by x_{ref} and is obtained in the previous step as the component of r_{ref} along the source array. The wavenumber, k_{peak} , wavepacket is obtained from the peak of the wavenumber spectrum of q_{part} , i.e., the spatial Fourier transform. This parameter describes the complex oscillations of the wavepacket and thereby its radiation angle. Once this process has been completed, the partial source is now described by just five parameters and its contribution can be removed from the full equivalent source.

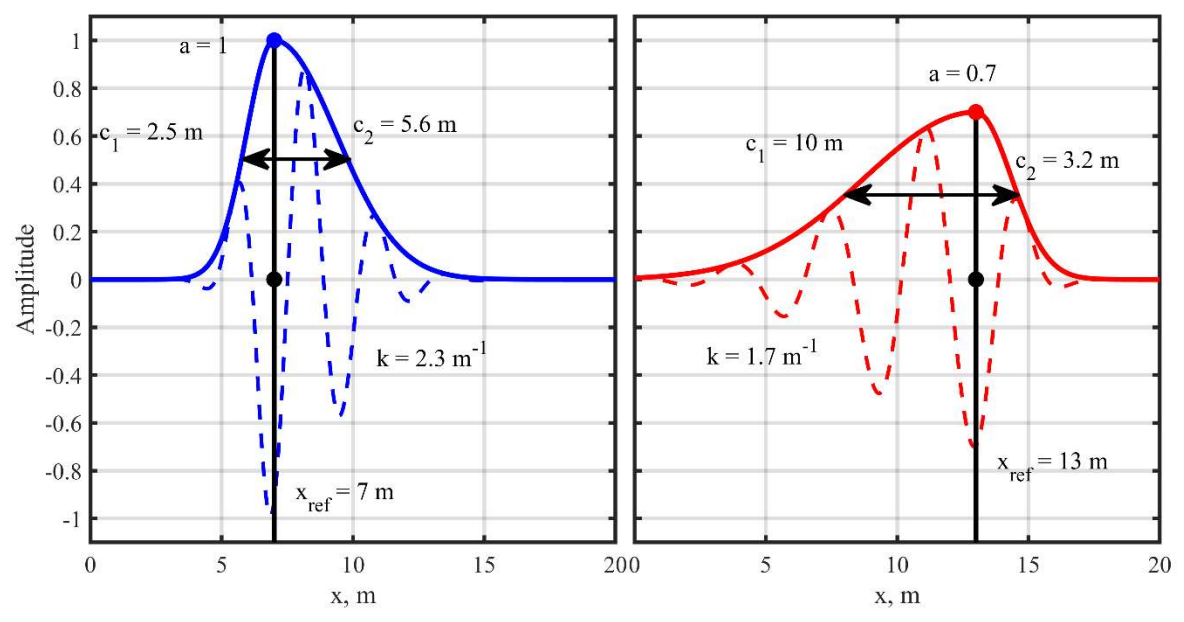


Figure 2. Examples of two wavepackets using different sets of parameters.

4. Update Q_z

The partial source defined by $q_{wpkt}(x)$ accounts for a portion of the coherent energy in \mathbf{Q}_z . Before generating the next wavepacket, this energy must be removed from the source model to ensure linear independence between wavepackets. This is done using a standard Graham-Schmidt process on each of the eigenvectors of \mathbf{Q}_z . Since this process will inevitably modify the singular values, it is prudent to recast the SVD in Eq. (13) as

$$\mathbf{Q}_{z} = \mathbf{W}\mathbf{W}^{\mathcal{H}},\tag{18}$$

where the singular values, $\mathbf{\Lambda} = Diag([\sigma_1, ..., \sigma_S])$ have been absorbed into the rescaled singular vectors, $\mathbf{W} = \mathbf{W} \mathbf{\Lambda}^{1/2} = [\mathbf{w}_1, ..., \mathbf{w}_S]$ with $\mathbf{w}_i = \sqrt{\sigma_i} \mathbf{w}_i$. For each of these scaled singular values, the projection of $\mathbf{q}_{wpkt} = \mathbf{q}_{wpkt}(\mathbf{r}_S)$ is removed as follows:

$$\boldsymbol{w}_{i}' = \boldsymbol{w}_{i} - \frac{\boldsymbol{q}_{wpkt}^{\mathcal{H}} \boldsymbol{w}_{i}}{\boldsymbol{q}_{wpkt}^{\mathcal{H}} \boldsymbol{q}_{wpkt}} \boldsymbol{q}_{wpkt}$$
(19)

These new singular vectors are then recombined in the style of Eq. (18):

$$\mathbf{Q'}_{z} = \mathbf{W'W'}^{\mathcal{H}},\tag{20}$$

where $\mathbf{W}' = [\mathbf{w}'_1, ..., \mathbf{w}'_S]$. This new cross-spectral matrix now represents the residual energy after excluding the contribution of \mathbf{q}_{wpkt} .

5. Repeat steps 2-4 as desired

The process for obtaining the next wavepackets is identical to the preceding steps, except now Q_z is replaced with Q'_z . At this point, the total number of wavepackets can either be prescribed or optimized according to an objective function. Generally, more wavepackets are required to represent a more complicated source. This is discussed further in Section V.

6. Optimize the set of wavepackets

The set of wavepackets, generated in the previous steps provides an analytic framework for describing the acoustical properties of the source. However, since the functions q_{wpkt} are only approximations to the partial sources q_{part} , this set does not form an orthogonal basis. To complete the decomposition and assign amplitudes, the set of wavepackets is now optimized. This is done by creating a set of linear equations to best match the set of scaled singular values of the original ESM:

$$\boldsymbol{Q}_{wnkt}\boldsymbol{\mathcal{C}} = \boldsymbol{\mathcal{W}}_0, \tag{21}$$

where $Q_{wpkt} = [q_{wpkt,1}, ..., q_{wpkt,n}]$ is the collection of wavepackets, $C \in \mathbb{R}^{n \times S}$ is the coefficient matrix describing the contribution of each wavepacket to the final source, and W_0 is the matrix of scaled singular vectors (see Eq. (18)) corresponding to the first iteration, i.e. when $Q_z = Q_{HM}$. This optimization is a straightforward application of linear-least squares with Tikhonov regularization for stability [24]

$$\mathbf{C} = \left(\mathbf{Q}_{wpkt}^{\mathcal{H}} \mathbf{Q}_{wpkt} + \delta \mathbf{I}\right)^{-1} \mathbf{Q}_{wpkt}^{\mathcal{H}} \mathbf{W}_{0}. \tag{22}$$

The identity matrix, **I** is scaled by the penalization parameter, δ . Finally, the reduced-order and scaled singular vectors are calculated as $\boldsymbol{w}_{red,i} = \boldsymbol{Q}_{wpkt} \boldsymbol{c}_i$ ($\boldsymbol{w}_{red} = [\boldsymbol{w}_{red,1}, ..., \boldsymbol{w}_{red,S}]$) where \boldsymbol{c}_i is the i^{th} column of \boldsymbol{c} and the reduced ESM is

$$\mathbf{Q}_{MPW}^{n} = \mathbf{W}_{red} \mathbf{W}_{red}^{\mathcal{H}}.$$
 (23)

Note that the index n has been added a superscript as a reminder that this model is created using n wavepacekts. The reduced-order ESM, \mathbf{Q}_{MPW}^n , is a source model that can be used in all the same ways as \mathbf{Q}_{HM} .

V. Results

This section provides validation of the multiple wavepacket decomposition as applied to the T-7A data. This section provides a sample decomposition at a peak frequency and discusses general properties observed. The application is then broadened to wavepacket behavior across frequency and how changing engine conditions impact the parameters. Finally, a single, frequency-dependent wavepacket is fit to the T-7A data.

An ESM is created via HM using the data collected from the T-7A measurement at military power (MIL). Spatially, the sources are placed at the jet centerline height and extend between -3 m and 30 m relative to the nozzle of the

aircraft with an inter-element spacing of 0.1 m. A mirrored image source is located beneath the aircraft to account for the pressure doubling seen by the ground-based microphones. After the HM processing, the image source is removed to simulate a free-field environment. Equivalent sources are created for frequencies between 51 and 600 Hz with a 3 Hz spacing, converted to their respective Strouhal numbers as $Sr = fD/u_j$, where f is the raw frequency, D is the jet exit diameter, and u_j is the jet exit velocity. This frequency range was chosen due to the limitations of HM processing. At higher frequencies, grating lobes begin to appear and reduce the quality of the results.

To demonstrate its validity, an example of the MWP decomposition is applied to the data collected at Sr = 0.12, which represents a peak frequency for the F404 jet at MIL. This frequency was decomposed using five wavepackets, which was chosen to visually distinguish the individual wavepackets as well as to show that adequate results are obtained using a relatively small number of basis functions. Figure 3 shows the results of the decomposition relative to the original model. The source strength (volume velocity) of the HM-educed ESM is shown in solid black at the left of the figure, and the source strengths from the MWP ESM are shown in red at the right. Individual wavepackets are shown in gray between the two with the magnitude in solid and the real part as a dashed line with number on the lower axis. One feature of the decomposition (as with most) is that the first wavepacket captures the most prominent part of the full-rank source distribution and each subsequent wavepacket accounts for higher-order terms. As with any expansion, including more terms enhances the fidelity of the approximation.

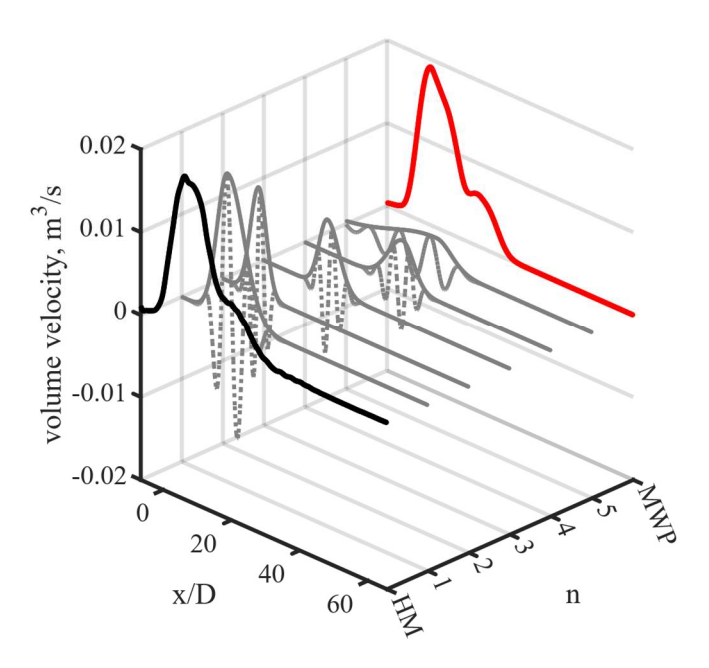


Figure 3. Sample MWP decomposition of the HM-derived ESM for MIL at Sr = 0.12.

From the ESM, field reconstructions are created using Eq. (12) to predict the pressure in the jet near field. Figure 4 shows the top 30 dB of these total field reconstructions using a) Q_{HM} and b) Q_{MWP}^5 . A model of the T-7A is included for scale and orientation (see Fig. 1). At Sr = 0.12, the noise exhibits a multi-lobed radiation phenomenon, an effect that is also captured by the MWP decomposition. The difference between the two maps is remarkably small. Figure 4c shows the difference between the two models. The largest disagreement is in the forward direction; however, for this frequency, the forward radiation is less than 30 dB below the maximum and is irrelevant. To account for this type of radiation, Papamoschou et al. [15] and later Harker [17] suggest that an incoherent monopole be included in the source model that is optimized to replicate the omnidirectional component of jet noise, though this is not included in this analysis. The two methods are much closer in the primary radiation direction with minimal error across this region. To provide a more quantitative metric of the error, a 20 dB down contour is included in each figure and the mean absolute error (MAE) is computed across this region (see 4c). For this frequency, the MAE is computed as 0.36 dB.

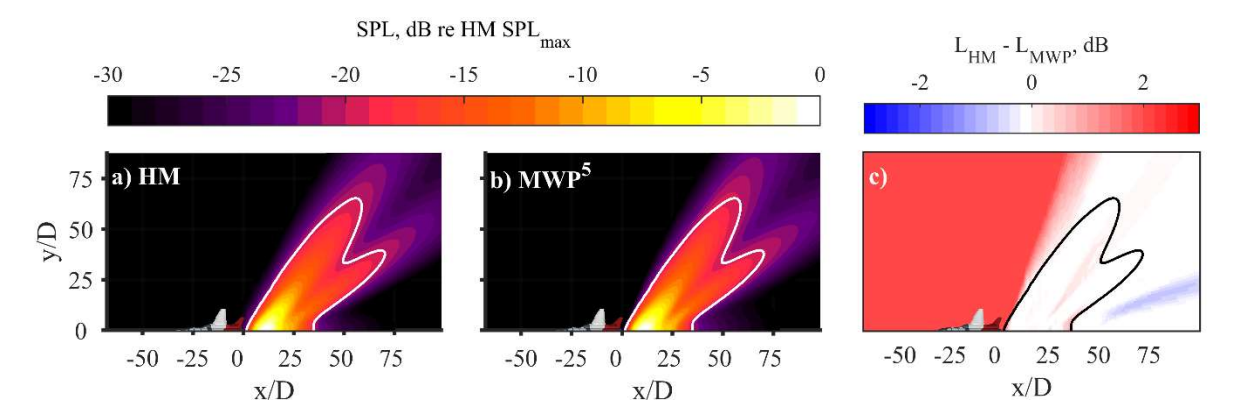


Figure 4. Total-field reconstructions produced by a) Q_{HM} and b) Q_{MWP}^5 as well as c) their difference. The white/black contours indicate the HM 20 dB down region where the MAE is calculated

Using HM, an ESM is created for each frequency at each engine condition, and the MWP decomposition is applied using between 1 and 10 wavepackets. Using the same process as in Fig. 4, the error for each frequency and wavepacket combination is calculated and the results plotted as a colormap in Fig. 5. Included in each subplot is a white contour demarking the 0.5 dB MAE line. These four engine conditions represent subsonic (38% thrust), transonic (55% thrust), and supersonic conditions (MIL and AB). The best results are seen at MIL (5c) and AB (5d) where the errors remain relatively small for a few wavepackets, even at higher frequencies. The error generally increases with frequency, which is consistent with increasing source complexity. This is also seen in the comparison between MIL and AB where the general error trends are the same, just slightly elevated. Of particular note are the bright patches near Sr = 0.12, 0.21, 0.30 with one wavepacket at MIL and similar features at AB. The reason for this increased error is due to a radiation feature observed in noise from full-scale jets that have come to be known as the spatiospectral lobes [25]. The lobes have been identified as a dual-lobe radiation pattern in field reconstruction (see Fig. 4), multiple peaks in microphone spectra at a single location, or as regions of local maxima in spatiospectral maps. While the physical mechanism behind the lobes is still being investigated, their spatial, spectral, and temporal properties have been studied [19,26]. While the lobes will not be discussed in depth here, their presence as a critical feature to noise radiation is noted. At 38% thrust (Fig. 5a), the errors grow significantly faster than the supersonic engine conditions. This is a little surprising, since 38% thrust represents a subsonic engine condition and, by extent, a simpler jet. One explanation is that the decomposition is designed to describe wavepacket-like structures. While wavepackets are present at subsonic engine conditions, they require a temporal jitter to accurately model field radiation [13]. Spectrally, the jitter would manifest as a coherence decay in the source description. However, coherence has not been included as a parameter since jitter is relatively unimportant for supersonic jets [13,27]. Thus, the wavepacket ansatz presented in Eq. (17) does not represent a natural basis for a subsonic jet. At 55% thrust (5b), the jet is transonic and exhibits some of the large error effects observed at 38% thrust, but not to the same extreme. Additionally, the presence of an additional radiation lobe begins to appear near Sr = 0.19.

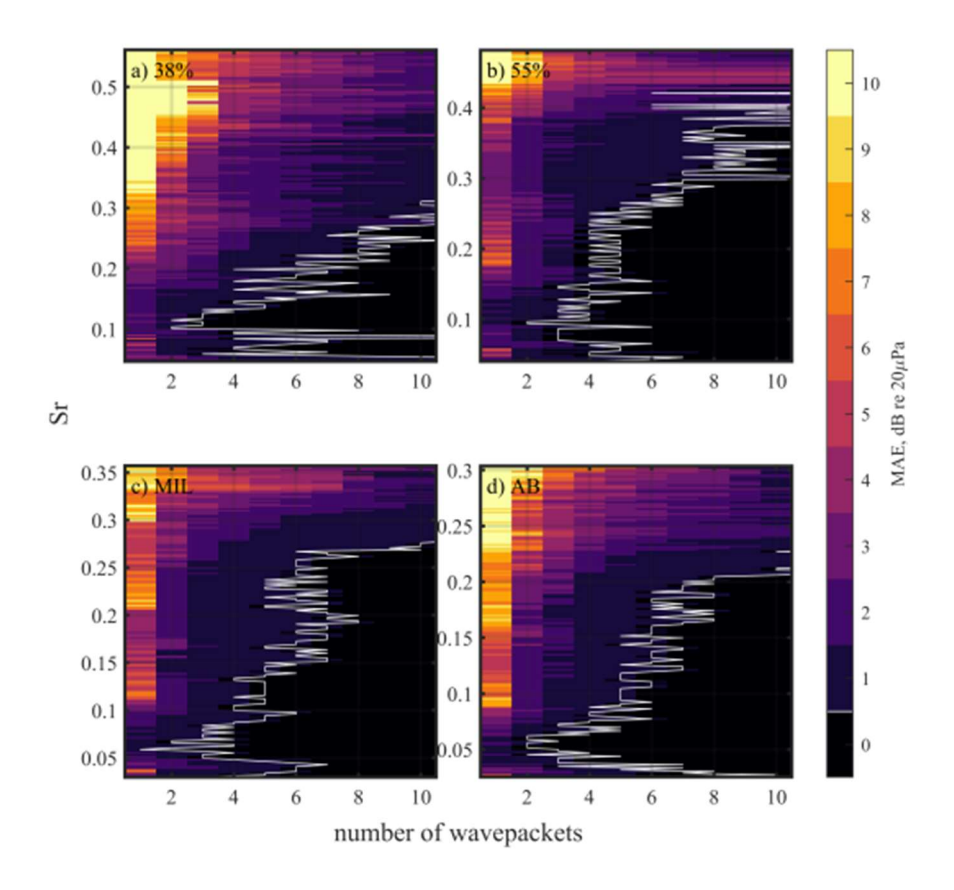


Figure 5. Mean absolute error (MAE) of the 20 dB down region as a function of engine condition, frequency, and number of wavepackets. A white 0.5 dB error contour is also included.

The white contours from Fig. 5 are reproduced in Fig. 6 as blue curves, this time with frequency along the abscissa and the number of wavepackets along the left ordinate. These curves demonstrate the number of wavepackets required to produce the field radiation to within 0.5 dB. As noted above, this form of the wavepacket decomposition is illsuited to describing subsonic radiation, so it is no surprise that the number of wavepackets needed for 38% thrust (6a) increases more rapidly than the other conditions. For each of the other conditions, the number of wavepackets remains relatively constant before suddenly spiking. At 55% thrust (6b), between 5 and 8 wavepackets are needed to represent Strouhal numbers up to 0.35, at MIL (6c) between 4 and 7 are required up to Sr = 0.26, at AB (6d) between 5 and 8 are needed up to Sr = 0.2. Included in each figure is an orange curve that normalizes the number of wavepackets by wavelength. For each engine condition (excluding 38% thrust), the number of wavepackets per wavelength increases somewhat linearly at low Strouhal numbers. This growth is slowest at 55% thrust and fastest at AB, which again indicates that the source becomes more complex with increasing engine condition. Additionally, since each wavepacket represents a self-coherent packet of energy, the source across all engine conditions becomes less coherent with increasing frequency. After this steady growth, the number of wavepackets exhibits a sudden spike. This occurs after peak radiation frequencies, which suggests that the source coherence deteriorates quickly after the peak radiation region. This same behavior was observed by Harker et al. [5] who showed that, for a full-scale supersonic jet, the axial source coherence lengths drop off rapidly past the peak frequencies. Similarly, Leete et al. [28] observed that the azimuthal coherence lengths decayed rapidly beyond the peak frequencies.

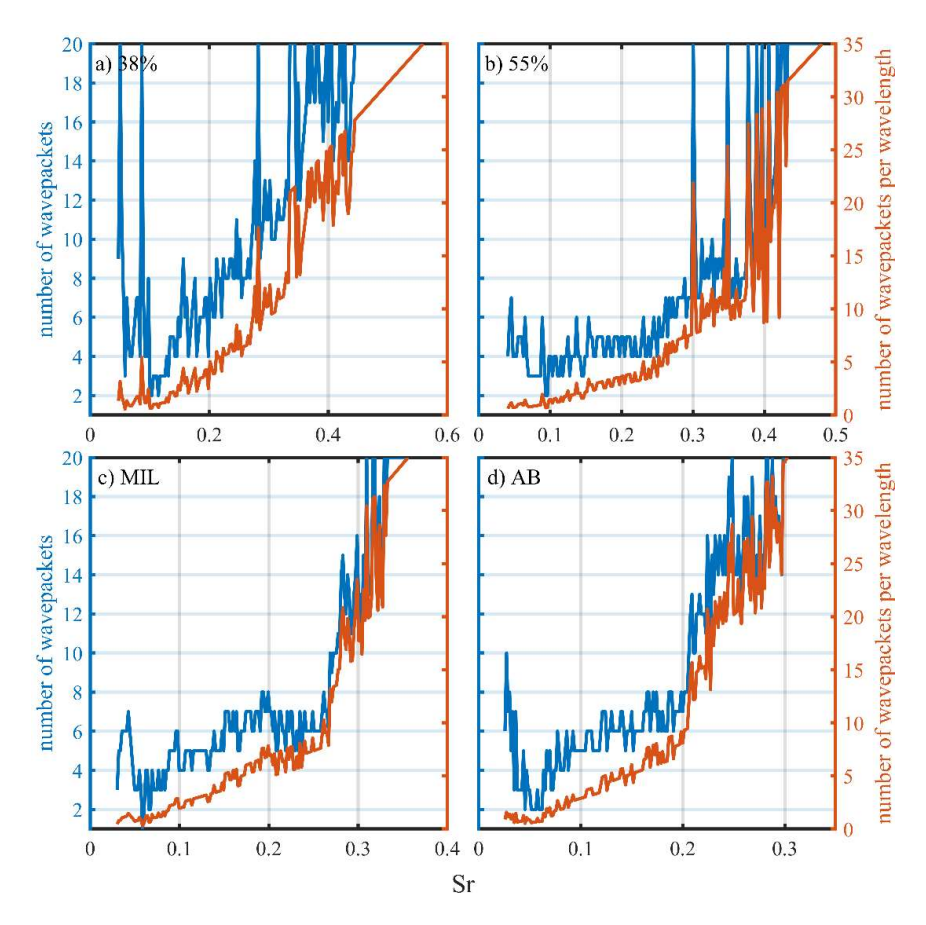


Figure 6. The number of wavepackets required to reconstruct the field radiation to within less than 0.5 dB. The orange curve is normalized by the acoustic wavelength.

Once the decomposition has been completed, the radiation fields generated by the individual wavepackets can be explored. Figure 7 shows examples of the MWP decomposition applied to Strouhal numbers of 0.059, 0.12, 0.18, 0.22, and 0.29. These frequencies were chosen as they represent the field radiation at low, mid, and high frequencies as well as when multi-lobed radiation is present and when it is not. The leftmost column shows the field reconstruction as predicted by the HM model. Subsequent columns correspond to the three most energetic wavepackets as determined by their sound power, which is included in the upper left corner of each subplot. The wavepacket fields are plotted relative to the maximum sound pressure level from the HM field reconstruction, which is included in the upper left corner of the HM subplot. Of note is the presence of multilobe radiation behavior characteristic of the spatiospectral lobes. Following the naming convention of Olaveson and Gee [19], Fig. 7a (Sr = 0.059) contains a single radiation lobe which is identified as lobe 1; 7f (Sr = 0.12) has lobes 1 and 2, where lobe 2 is more to the sideline and lobe 1 is fainter beneath it; 7i (Sr = 0.18) includes lobes 2 and 3, with lobe 3 being farther to the sideline; 7n (Sr = 0.22) has lobes 3 and 4; and 7r (Sr = 0.29) lobes 4 and 5. For the most part, the primary radiation lobe is captured by the first wavepacket and any secondary lobe by the second. However, this is not true at Sr = 0.12. At this frequency, lobe 2 is captured by the first wavepacket, but the second wavepacket does not correspond to lobe 1. In fact, none of the later wavepackets have the same directivity and it is only after combining the next few wavepackets that lobe 1 manifests. The fact that the higher-ordered lobes are represented by a single wavepacket while lobe 1 requires a superposition of multiple is further evidence that its production mechanism is different from the others as discussed in Leete [26] and Olaveson and Gee [19]. Given that lobe 1 has a directivity angle of roughly 150 degrees (see 7a) it is likely related to subsonic radiation see Ref. [21].

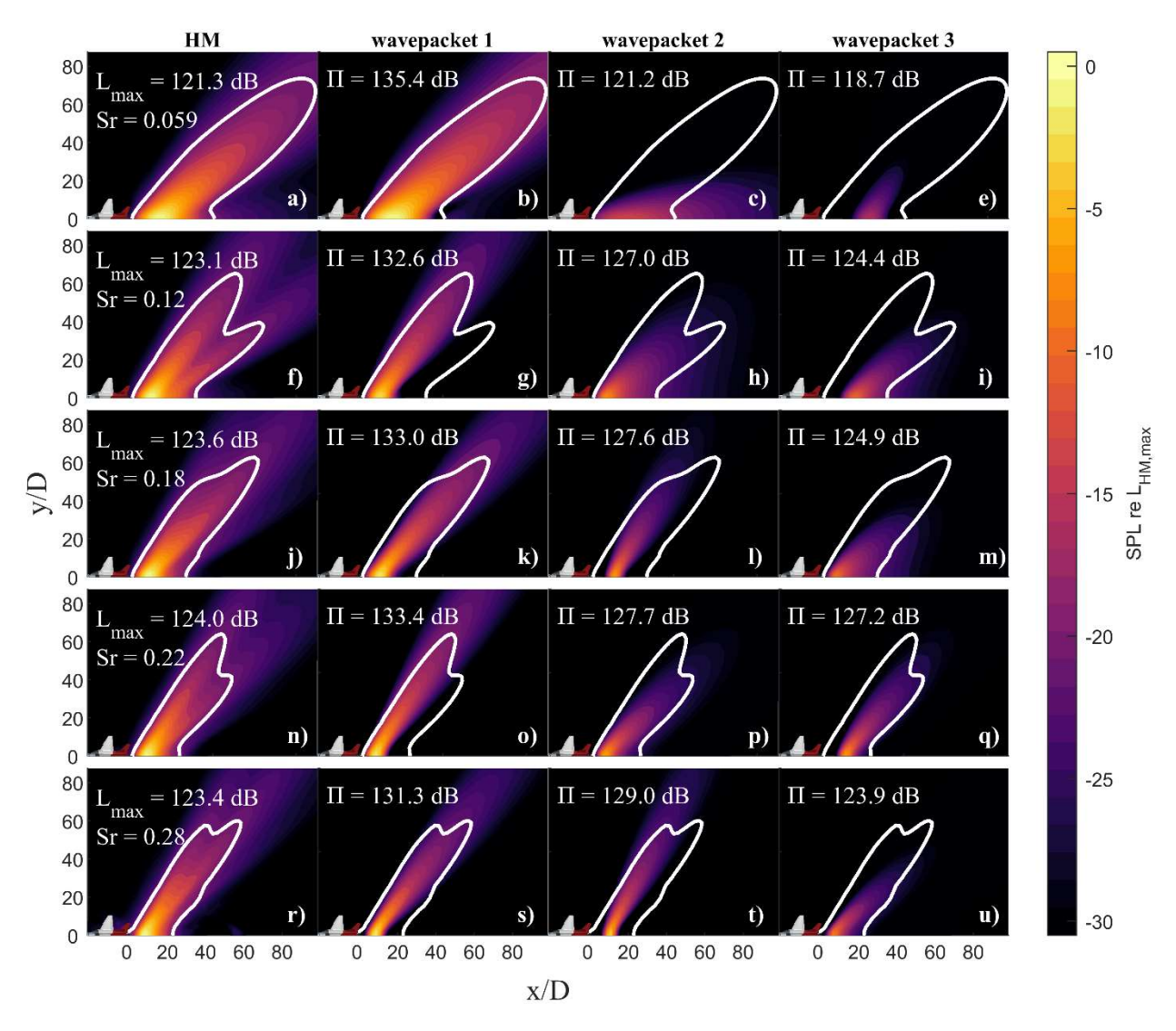


Figure 7. Field decompositions by wavepacket for five frequencies. Columns correspond to individual wavepackets while rows correspond to frequencies. The sound power of each wavepacket is listed in the top left corner of each subplot and the white contour identifies the 20 dB down region of the HM reconstruction.

While it is desirable to represent the entire source decomposition as a collection of wavepackets with frequencydependent parameters, the difficulty in tracking each wavepacket as it evolves through a 5-dimensional parameter space makes interpolation impossible with the current decomposition method. As an alternative, the parameters for a single wavepacket representation of the source are depicted in Fig. 8. The amplitude curve (8a) suggest that the primary radiation lobe becomes more dominant with increasing frequency and that more energy is contained in the high frequencies, which is consistent with jet noise literature. The wavepacket centers (8b) are seen to start downstream and slowly move upstream with frequency, which is again consistent. The growth and decay rates (8c and d) both follow an approximate exponential decay with a few jumps in the decay rate. Since these rates are representative of the width of the wavepacket and each wavepacket is self-coherent, it again demonstrates the decreasing coherence length with increasing frequency. For the peak wavenumber (8e), the curve generally tends upward. This parameter is intrinsically tied to the radiation angle and demonstrates that the primary radiation lobe shifts towards the sideline with increasing frequency. The discontinuities at $Sr \approx 0.12, 0.21, 0.30$ are not artifacts of the processing, but identify the transition regions between spatiospectral lobes (see Fig. 7). These transition regions happen when the dominant lobe slowly fades out and is overtaken by a secondary lobe. These properties have been observed in previous full-scale analyses (see Leete at al. [26]) and are consistent. Finally, Fig. 8f shows the error between the single wavepacket and the full-rank model. At low frequencies, there is little error between the two predictions, however at the same frequencies as before, the error is seen to increase sharply. This indicates the dual lobed radiation phenomenon that is unable to be adequately captured by a single wavepacket. As frequency grows, so does the error, which again, tells about the complicated nature of the source. In all, a single-wavepacket model can approximate the salient features of the dominant radiation lobe, but is unable to capture all the complexity of the full source. Similar limitations have been seen in other single-wavepacket decompositions, such as the intensity-based model presented by Whiting et al. [29].

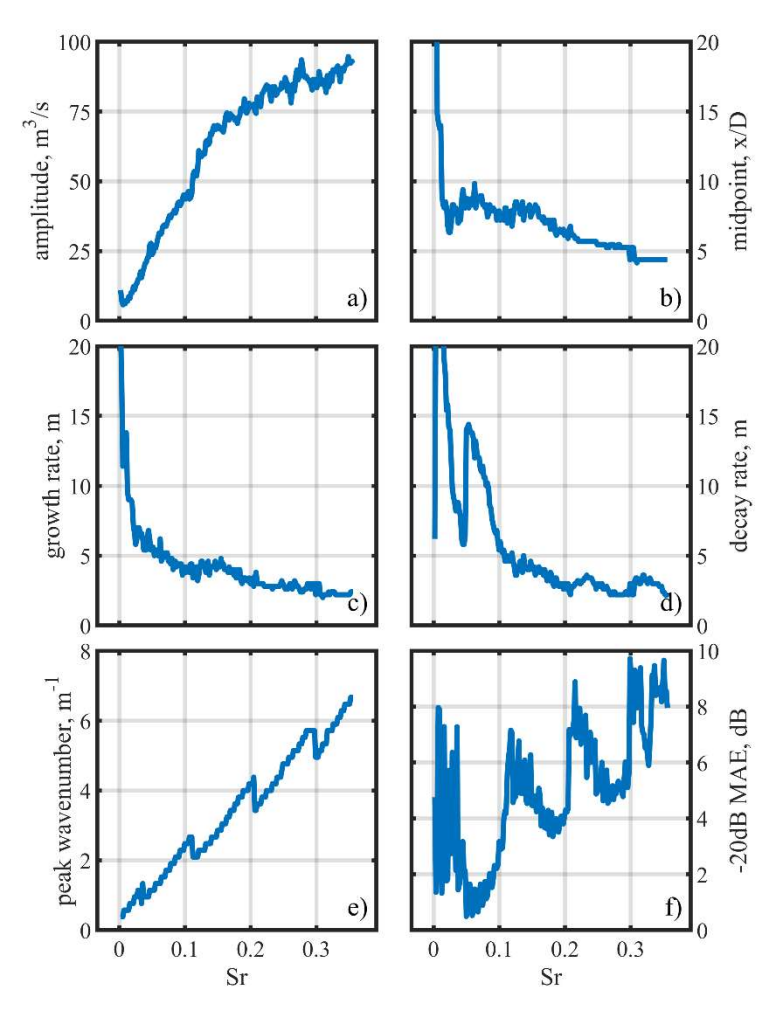


Figure 8. Parameters as a function of frequency for a single wavepacket describing the primary radiation lobe.

VI. Conclusion

This study represents the first application of a multiple wavepacket decomposition to a new full-scale aircraft. The process reduces the full-rank equivalent source model produced by hybrid beamforming to a collection of analytic wavepackets. For a remarkably small number of parameters, the same source distribution and field radiation can be obtained to within less than 0.5 dB of average error. For subsonic engine conditions, turbulent wavepackets require some degree of temporal jitter (coherence decay) to match the same field radiation. As such, the decomposition is most suitable to supersonic engine conditions where self-coherent wavepackets form a suitable basis. For these conditions, the field radiation can be adequately captured with between 3 and 8 wavepackets across the dominant frequencies, which represents a significant reduction in model complexity. The relationship between individual wavepackets and the spatiospectral lobes has been explored, and it was shown that lobe 1 is the result of a superposition of wavepackets, whereas the higher-ordered lobes are associated with a single wavepacket. This again suggests that the production mechanism for lobe 1 is different than the others. Finally, the wavepacket parameters for a single wavepacket model are presented as a function of frequency. These parameters are consistent with the jet noise

literature and adequately describe the primary radiation lobe. The limitation to the single-wavepacket model is that it is unable to capture dual-lobed radiation, which is an important component of full-scale military jets.

Future work will focus on connecting the acoustic wavepackets derived here to the turbulent wavepackets observed in turbulence decomposition. Furthermore, alternative decomposition methods should be investigated to see if multiple frequency-dependent wavepackets can be constructed to better model the radiated noise at all frequencies.

- [1] Martens, S. and Spyropoulos, J. T., "Practical Jet Noise Reduction for Tactical Aircraft," *Proceedings of ASME Turbo Expo 2010*, 2010. https://doi.org/10.1115/GT2010-23699
- [2] Wall, A. T., Gee, K. L., Morris, P. J., Colonius, T., and Lowe, K. T., "Introduction to the special issue on supersonic jet noise", *The Journal of the Acoustical Society of America*, 151, 806, 2022. https://doi.org/10.1121/10.0009321.
- [3] Merino-Martinez, R., Sijtsma, P., Snellen, M., Ahlefeldt, T., Antoni, J., Bahr, C. J., Blacodon, D., Ernst, D., Finez, A., Funke, S., Geyer, T. F., Haxter, S., Herold, G., Huang, X., Humphreys, W. M., Leclère, Q., Malgoezar, A., Michel, U., Padois, T., Pereira, A., Picard, C., Sarradj, E., Siller, H., Simons, D. G., Spehr, C., "A review of acoustic imaging methods using phased microphone arrays," *CEAS Aeronautical Journal*, Vol. 10, pp 197-230, 2019
- [4] Padois, T, Gauthier, P-A, and Berry, A, "Inverse problem with beamforming regularization matrix applied to sound source localization in closed wind-tunnel using microphone array," *Journal of Sound and Vibration*, 333, 2014.
- [5] Harker, B. M., Gee, K. L., Neilsen, T. B., Wall, A. T., and James, M. M. "Source characterization of full-scale tactical jet noise from phased-array measurements," The Journal of the Acoustical Society of America, 146, 665, 2019. https://doi.org/10.1121/1.5118239
- [6] Olaveson, T., Ward, J. A., Johnson, J. P., Gee, K. L., and Wall, A. T., "Analysis of Spatiospectral Lobes in Installed F404 Engine Noise Radiation," 28th AIAA/CEAS Aeroacoustics 2022 Conference, June 14-17, 2022, Southampton, UK.
- [7] Weiss, J., "A Tutorial on the Proper Orthogonal Decomposition," AIAA Aviation 2019 Forum, 17-21 June, Dallas, Texas, 2019.
- [8] Schmidt, O. T., and Colonius, T., "Guide to Spectral Proper Orthogonal Decomposition," *AIAA Journal*, Vol 58, No. 3, 2020.
- [9] Schmidt, O. T., Towne, A., Rigas, G., Colonius, T., and Brès, G. A., "Spectral analysis of jet turbulence," *J. Fluid Mech.* Vol 855, pp. 953-982, 2018.
- [10] Towne, A., Schmidt, O. T., and Colonius, T., "Spectral proper orthogonal decomposition and its relationship to dynamic mode decomposition and resolvent analysis," *J. Fluid Mech.*, vol 847, pp. 821-867, 2018.)
- [11] Crow, S. C. and Champagne, F. H., "Orderly structure in jet turbulence," *Journal of Fluid Mechanics*, vol 48, pp 547-591, 1971.
- [12] Jordan, P. and Colonius, T., "Wave Packets and Turbulent Jet Noise," *Annual Review of Fluid Mechanics*, 45, 173-195, 2013
- [13] Cavalieri, A. V. G., Jordan, P., Agarwal, A., and Gervais, Y., "Jittering wave-packet models for subsonic jet noise," *Journal of Sound and Vibration*, 330 (2011), 4474-4492.
- [14] Akamine, M., Okamoto, K., Teramoto, S., and Tsutsumi, S., "Conditional sampling analysis of high-speed schlieren movies of Mach wave radiation in a supersonic jet," *JASA EL*, **145**, EL122, 2019. https://doi.org/10.1121/1.5088493
- [15] Papamoschou, D., "Wavepacket Modeling of the Jet Noise Source," 17th AIAA CEAS Aeroacoustics Conference, 05-08 Jun 2011, Portland, Oregon, AIAA Paper No. 2011-2835.
- [16] Whiting, E. B., Gee, K. L., Stout, T. A., Neilsen, T. B., Wall, A. T., and James, M. M., "A vector intesntiy-based equivalent wavepacket model for high-performance military aircraft jet noise," *Proc. Mtgs. Acoust.* **25**, 045007, 2015. Doi: https://doi.org/10.1121/2.0001236.
- [17] Harker, B. M., "Characterization of military aircraft jet noise using wavepacket analysis and other array processing methods", Ph.D dissertation, Brigham Young University, 2017.
- [18] Olaveson, T., Harker, B. M., and Gee, K. L., "Beamforming-based wavepacket model for noise predictions of tactical aircraft," *Proc. Mtgs. Acoust.* **29**, 040011, 2016.
- [19] Olaveson, T. W. and Gee, K. L., "Wavelet-Based Characterization of Spatiospectrotemporal Structure in F404 Engine Jet Noise," *AIAA J.* Vol 62, No. 11, 2024.
- [20] Mathews, L. T. and Gee, K. L., "Acoustical Holography and Coherence-Based Noise Source Characterization of an Installed F404 Engine," *AIAA J.* Vol 62, No. 6, 2024.
- [21] Gee, K. L., Olaveson, T. W., and Mathews, L. T., "Convective Mach Number and Full-Scale Supersonic Jet Noise Directivity," *AIAA J.* accepted Nov 2024.

- [22] Leete, K. M., Vaughn, A. B., Bassett, M. S., Rasband, R. D., Novakovich, D. J., Gee, K. L., Campbell, S. C., Mobley, F. S., and Wall, A. T., "Jet Noise Measurements of an Installed GE F404 Engine," *AIAA SciTech Forum*, 11-15 and 19-21 January 2021, virtual event, AIAA Pap No. 2012-1638.
- [23] Schmidt, R. "Multiple emitter location and signal parameter estimation," *IEEE transactions on antennas and propagation* **34**, 276-280, 1986
- [24] Padois, T., Berry, A., and Gautheir, P-A., "Beamforming matrix regularization and inverse problem for sound source localization: Application to aero-engine noise," 19th AIAA/CEAS Aeroacoustics Conference, May 27-29, 2013, Berlin Germany.
- [25] Wall, A. T., Gee, K. L., Neilsen, T. B., Harker, B. M., McInerny, S. A., McKinley, R. L., and James, M. M., "Investigation of multi-lobed fighter jet noise sources using acoustical holography and partial field decomposition methods," 21st AIAA/CEAS Aeroacoustics Conference, 22-26 June 2015, Sallas, TX, 2015
- [26] Leete, K. M., Wall, A. T., Gee, K. L., Neilsen, T. B., James, M. M., and Downing, J. M., "Acoustical Holography-Based Analysis of Spatiospectral Lobes in High-Performance Aircraft Jet Noise," *AIAA J.* Vol. 59, No. 10, 2021.
- [27] Cavalieri, A. V. G. and Agarwal, A. "Coherence decay and its impact on sound radiation by wavepackets," *J. Fluid Mech.*, vol 748, pp399-415, 2014.
- [28] Leete, K. M., Wall, A. T., Gee, K. L., Neilsen, T. B., Harker, B. M., and James, M. M., "Azimuthal coherence of the sound field in the vicinity of a high performance military aircraft," *Proc. Mtgs. Acoustic.* **29**, 045007, 2016. [29] Whiting, E. B., Gee, K. L., Stout, T. A., Neilsen, T. B., Wall, A. T., and James, M. M., "A vector intesntiy-based equivalent wavepacket model for high-performance military aircraft jet noise," *Proc. Mtgs. Acoust*, **25**, 045007, 2015.